

# Visualizing the Carbon Binder Phase of Battery Electrodes in Three Dimensions

Sohrab R. Daemi,<sup>†</sup> Chun Tan,<sup>†</sup> Tobias Volkenandt,<sup>‡</sup> Samuel J. Cooper,<sup>§</sup> Anna Palacios-Padros,<sup>||</sup> James Cookson,<sup>||</sup> Dan J. L. Brett,<sup>†</sup> and Paul R. Shearing<sup>\*,†,||</sup>

<sup>†</sup>Electrochemical Innovation Lab, Department of Chemical Engineering, University College London, London WC1E 7JE, United Kingdom

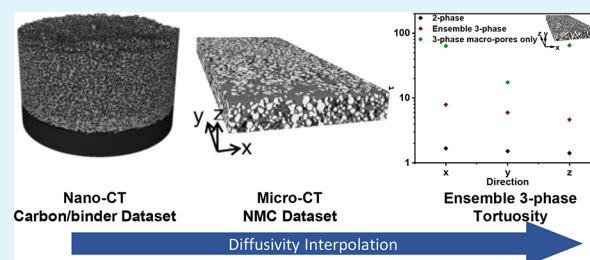
<sup>‡</sup>Carl Zeiss Microscopy GmbH, Oberkochen 73447, Germany

<sup>§</sup>Dyson School of Design Engineering, Imperial College London, South Kensington, London SW7 2AZ, United Kingdom

<sup>||</sup>Johnson Matthey Technology Centre, Blounts Court Road, Sonning Common, Reading RG4 9NH, United Kingdom

**ABSTRACT:** This study presents a technique to directly characterize the carbon and binder domain (CBD) in lithium-ion (Li-ion) battery electrodes in three dimensions and use it to determine the effective transport properties of a Li-Ni<sub>0.33</sub>Mn<sub>0.33</sub>Co<sub>0.33</sub>O<sub>2</sub> (NMC) electrode. X-ray nanocomputed tomography (nano-CT) is used to image an electrode composed solely of carbon and binder, whereas focused ion beam–scanning electron microscopy is used to analyze cross-sections of a NMC electrode to gain morphological information regarding the electrode and CBD porosity. Combining the information gathered from these techniques reduces the uncertainty inherent in segmenting the nano-CT CBD data set and enables effective diffusivity of its porous network to be determined. X-ray microcomputed tomography (micro-CT) is then used to collect a NMC data set that is subsequently segmented into three phases, comprised of active material, pore, and CBD. The effective diffusivity calculated for the nano-CT data set is incorporated for the CBD present in the micro-CT data set to estimate the ensemble tortuosity factor for the NMC electrode. The tortuosity factor greatly increases when compared to the same data set segmented without considering the CBD. The porous network of the NMC electrode is studied with a continuous pore size distribution approach that highlights median radii of 180 nm and 1 μm for the CBD and NMC pores, respectively, and with a pore throat size distribution calculation that highlights median equivalent radii of 350 and 700 nm.

**KEYWORDS:** Li-ion batteries, lab-based X-ray computed tomography, carbon binder characterization, porous materials, multiscale image-based modeling



## 1. INTRODUCTION

Li-ion batteries have emerged as the preferred choice for energy storage applications that require high energy and power densities, such as consumer electronics and electric vehicles (EVs).<sup>1</sup> However, significant advances are still required in performance, safety, and lifetime to enable greater penetration of EVs into the market.

The performance of a Li-ion battery is intrinsically linked to the microstructure of its electrodes. The electrochemical reactions within these devices occur in porous electrodes comprised of active material particles, typically a transition metal oxide, mixed with conductive carbon and binder and coated on a metallic current collector.<sup>2</sup> The conductive carbon and binder forms a porous network around the active material particles, known collectively as the CBD. The main function of the CBD is to aid electrical conduction from the current collector to the active material particles, while the binder ensures structural integrity and good electrical contact of the electrode through adhesion with the current collector.<sup>2</sup> At the same time, ionic

conduction occurs through the electrolyte-filled pore space and within each of the active particles.<sup>3</sup>

Commonly studied metrics, such as porosity and tortuosity, are fundamental for a thorough understanding of how different species travel within electrodes, and these are governed not only by the chemical properties of the specific material but also by the morphology of the medium they are traveling through.<sup>4</sup> The tortuosity factor, for example, allows the relationship between morphology and the effective ionic diffusivity of the electrode pore network to be investigated. Throughout the past few decades of battery research, there has been growing interest in battery modeling as a tool to describe the operation and performance of Li-ion batteries. The Newman model, first proposed by Newman et al., was based on the assumption of spherical electrode particles and 1D transport of Li ions and electrons and has emerged as a prominent way to model battery

Received: March 28, 2018

Accepted: June 29, 2018

Published: July 20, 2018

performance.<sup>5</sup> These macro-homogeneous models often make empirical assumptions on effective transport parameters such as the Bruggeman correlation, relating the tortuosity of an electrode to its porosity. However, there are significant limitations inherent in these models, as they do not account for heterogeneities that can lead to accelerated degradation, where variations in local tortuosity may result in different states of charge (SoC) throughout the electrode.<sup>6</sup>

A range of novel microstructural characterization techniques, such as scanning electron microscopy (SEM),<sup>7–9</sup> focused ion beam–SEM (FIB-SEM),<sup>10–13</sup> electrochemical strain microscopy,<sup>14–16</sup> and X-ray computed tomography (X-ray CT),<sup>17–21</sup> have been applied to investigate the structure–property relationships of electrode materials, in order to improve the understanding of the impact of electrode microstructure on the performance of electrochemical devices as a whole. In particular, X-ray CT has emerged as a versatile, nondestructive, multi-length scale tool that has been used for a variety of studies that range from the observation of degradation-related phenomena<sup>22,23</sup> to the characterization of various electrode microstructures<sup>24,25</sup> and how these affect the overall performance of the battery.

X-ray CT operates by analyzing the attenuation caused by a sample to an incident X-ray beam.<sup>26,27</sup> The extent of X-ray attenuation is highly dependent on the atomic number or density of the imaged material, leading to an inherent limitation of this technique in characterizing low-Z materials such as the CBD in Li-ion electrodes. The contrast ratio resulting from disparate X-ray attenuation obtained by adjacent phases of very different densities renders low-attenuating materials such as the CBD indiscernible in the final image. Due to this, the CBD has been segmented as a completely porous phase in the majority of recent related studies.<sup>19,25,28–30</sup> While general observations can be made regarding transport parameters within an electrode, assuming that the entirety of the inactive phase acts as a porous pathway significantly lowers the measured tortuosity factor.

The CBD has previously been visualized or modeled in three dimensions via a combination of X-ray CT, FIB-SEM, and computational modeling.<sup>31,32,11</sup> The first attempt by Hutzenlaub et al. segmented a previously collected FIB-SEM data set of a lithium cobalt oxide (LCO) electrode in three phases, highlighting the difference in measured transport properties when the CBD is taken into consideration. Zielke et al. inscribed a “virtual” CBD within the pore space segmented from a micro-CT data set of an LCO electrode using two different models, namely, a random cluster model and a fiber model.<sup>33</sup> A later study by Zielke et al. takes the previous work one step further by stochastically modeling the CBD based on seven slices of a FIB-SEM data set and imposing this on a larger micro-CT volume of the same electrode.<sup>34</sup> Despite the high spatial resolution achievable with FIB-SEM, its destructive nature and the laborious and lengthy acquisition process poses a limit in collecting a data set that can be deemed representative.

To further improve the understanding of the role that the inactive phase plays within an electrode, novel methods are required to acquire representative data sets to model the carbon and binder accurately. To this end, this work proposes, for the first time to the authors’ knowledge, a method to directly image the CBD with lab-based Zernike phase contrast X-ray nano-CT. This technique couples sub-micrometer resolution with large analyzable subvolumes (ca.  $2.6 \times 10^4 \mu\text{m}^3$ ) obtainable in a fast and high-throughput workflow. The porosity and effective diffusivity of the CBD was computationally determined from a

nano-CT data set and superimposed onto a micro-CT data set of a lithium nickel manganese cobalt oxide (NMC) electrode to study how the transport properties and pore size distributions are affected by the inclusion of the CBD. FIB-SEM is also used to reduce the uncertainty relative to the data analysis by offering a ground-truth segmentation that confirms the calculated porosity.

Transport parameters, such as the tortuosity factor, were calculated with the MATLAB plugin TauFactor,<sup>35</sup> which solves the steady-state diffusion equation between two Dirichlet boundary conditions in a binarized volumetric data set. This allows for an effective diffusion coefficient,  $D_{\text{eff}}$  to be calculated, based on eq 1:

$$D_{\text{eff}} = D \frac{\phi}{\tau} \quad (1)$$

where  $D$  is the intrinsic diffusivity of the relevant transporting phase;  $D_{\text{eff}}$  is the effective diffusivity through the porous volume of interest;  $\phi$  is the volume fraction of the conductive phase of interest; and the tortuosity factor,<sup>35</sup>  $\tau$ , is determined by comparing the steady-state diffusive flow in a fully porous control volume to that obtained in a porous network with the same diffusivity and size. As the diffusive flow considered in this work is occurring exclusively via the porous network,  $\phi$  will be replaced by the porosity  $\varepsilon$  in all following tortuosity equations.

Since the diffusivity for the pores in this study is set arbitrarily to  $D_{\text{pore}} = 1 \text{ m}^2 \text{ s}^{-1}$ , a dimensionless diffusivity  $D^*$  is defined as presented in eq 2:

$$D^* = \frac{D}{D_{\text{bulk}}} = \frac{\varepsilon}{\tau} \quad (2)$$

The work presented here combines high-resolution FIB-SEM data with more representative nano-CT data by relying on microstructural information directly collected from a carbon and binder coating. While FIB-SEM can offer a factor of ca. 5 improvement in resolution, nano-CT presents a higher throughput and more repeatable technique for generating representative CBD volumes. The synergetic application of nano- and micro-CT with FIB-SEM offers advantages on both length scales. On the nano-scale, the combined use of these techniques allows for an increased accuracy when determining the porosity and reducing the uncertainty associated with segmenting the data. On the micro-scale, FIB-SEM allows drawing qualitative conclusions on the morphology and distribution of macro-pores aiding in the segmentation of the NMC data set in three phases.

A summary of this approach is detailed as follows:

(1) A pillar composed solely of carbon and binder was imaged with Zernike phase contrast X-ray nano-CT and segmented over a range of grayscale threshold values. The expected porosity of the layer was determined from a priori mass loading calculation and FIB-SEM slices. This was then used to determine the porosity of the CBD by selecting the corresponding grayscale value within a visually realistic range. The effective diffusivity,  $D_{\text{eff}}$  was then determined by using TauFactor.

(2) Several trenches were milled into the NMC electrode using FIB-SEM. From these, 12 slices imaging solely carbon and binder were extracted and their average porosity was measured.

(3) X-ray micro-CT was used to image the full NMC electrode, and the data set was segmented into two and three phases: in the two-phase segmentation, the NMC particles are segmented and the rest is treated as pore; in the three-phase

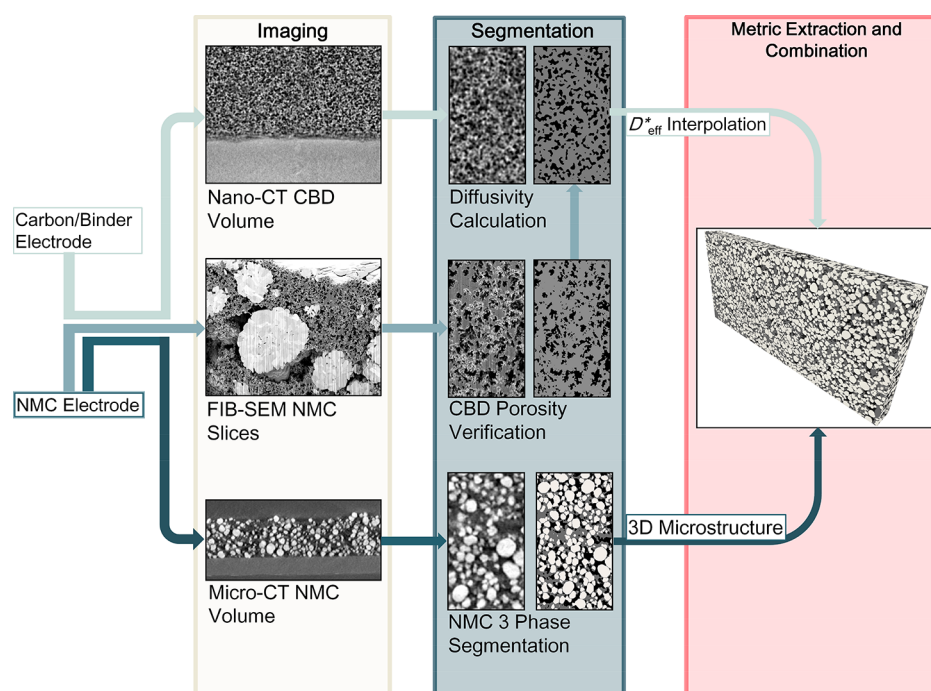


**Figure 1.** Schematic illustrating the analysis workflow developed in this study. Imaging of the electrode disk solely composed from carbon and binder was performed with nano-CT, while an NMC electrode was imaged in parallel using a combination of FIB-SEM and micro-CT. Finally, the information from these routes was combined into a single numerical analysis.

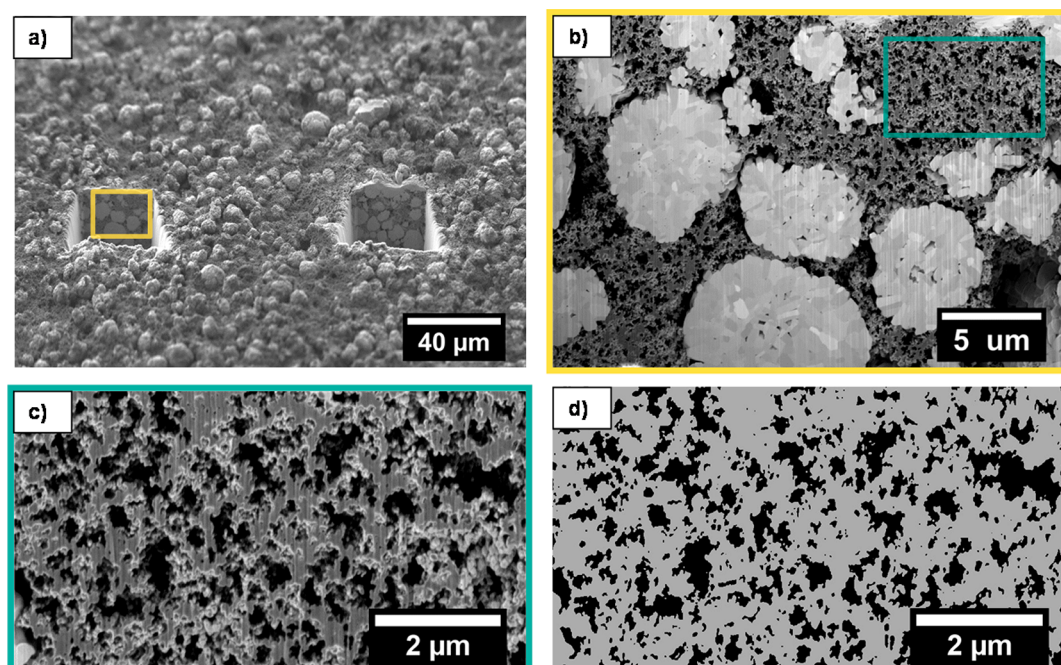


**Figure 2.** (a) SEM micrograph taken at 500 $\times$  depicting two of the trenches milled into the NMC electrode. The yellow box depicts the area of focus of the serial sectioning. (b) SEM micrograph taken at 4000 $\times$  depicting the electrode with the green box outlining the CBD slice used successively. (c) Closeup of the SEM micrograph in panel b. (d) Threshold segmentation of the image in panel c.

segmentation the particles were segmented separately from the CBD and macro-porous electrode porosity. Subsequently, a fully internal volume was extracted, and the effective diffusivity was then determined by using TauFactor.

This workflow is represented schematically in Figure 1.

## 2. RESULTS AND DISCUSSION

First, we calculated the effective diffusivity of the independent CBD electrode. The nano-CT derived CBD data set was threshold segmented with volume fraction information extracted from higher resolution FIB-SEM imaging.

Figure 2 presents an example of a trench from which a magnified SEM micrograph was obtained. A pixel size of 9.3 nm

proved sufficient to visualize the distribution of particles, pores, and binder. Two porosity domains are identifiable from Figure 2b, namely, nano-scale CBD pores and electrode macro-pores formed by gaps between particles. In the context of battery operation, both length scales of porosity are thought to play an important role.<sup>36</sup> Larger pores are thought to be formed by both gas bubbles trapped in the electrode slurry during drying and also by the slurry itself stretching around particles that act as fixed points. The finer CBD porosity is thought to be formed by gaps between carbon clusters as well as finer micro- and mesopores within the carbon particles that cannot be detected with the FIB-SEM resolution. Both porosities are important as they are responsible for providing pathways for Li-ion transport. Furthermore, the larger pores are also thought to facilitate the wetting of the electrode and active material.<sup>36,37</sup>

The green outline in Figure 2b displays an example of a CBD region which is successively segmented with thresholding as displayed in Figure 2c,d. A first estimate of the CBD porosity was obtained after thresholding 12 such CBD subsections into pore and carbon, yielding an average porosity of  $27 \pm 3\%$ .

Subsequently, a grayscale sensitivity analysis was performed on the nano-CT CBD data to determine the best grayscale for accurate porosity representation. The theoretical porosity of the electrode was calculated by using eq 3:

$$\varepsilon_{\text{theoretical}} = 1 - \frac{\rho_{\text{electrode}}}{\rho_{\text{CB}}} \quad (3)$$

where  $\rho_{\text{electrode}}$  is the measured density of the electrode calculated from the mass of the electrode and  $\rho_{\text{CB}}$  is the theoretical electrode density calculated from the density of all the phases weighted by volume fraction. To calculate  $\rho_{\text{CB}}$ , the density for C65 was assumed to be  $0.16 \text{ g cm}^{-3}$ , which corresponds to the density provided by manufacturer specification.<sup>38</sup> This value accounts for the porosity intrinsic to the carbon black particles that are below the spatial resolution of nano-CT.<sup>39</sup> From these calculations, we have found the expected porosity to be 28% for the carbon and binder electrode.

An internal subvolume  $16.7 \times 40.6 \times 38.9 \mu\text{m}^3$  was extracted from the nano-CT data set; estimates of reasonable grayscale threshold boundaries were obtained by visually identifying the pores. The histogram in Figure 3b does not present a bimodal distribution, therefore reinforcing the need for a sensitivity analysis achieved by combining the FIB-SEM data as ground-truth segmentation to determine the correct grayscale threshold for segmenting the nano-CT data set. The reconstructed images were 16-bit (i.e., 0–65535); however, the utilized range (i.e., the range of values resulting from the reconstruction process containing both the solid and pore phases) was approximately 18000–30000. Voxels at the boundaries between two phases may belong to more than a single phase due to the partial volume effect, as such there is always some uncertainty in segmenting the interfacial regions between solid and pore. Hence a range of “visually realistic” grayscale values is chosen between 21100 and 21600 via thresholding. Within these boundaries the calculated porosity ranges between 31 and 27%.

The average value between the porosity calculated with the FIB-SEM data and the theoretical porosity calculated for the CBD was 28%. This is used to select a threshold value of 21200 for segmenting the carbon and binder data set resulting in a segmented porosity of 27.6%, which is in agreement with the previous considerations. These ranges can be viewed in Figure 3a. The resulting segmentation obtained on the carbon and

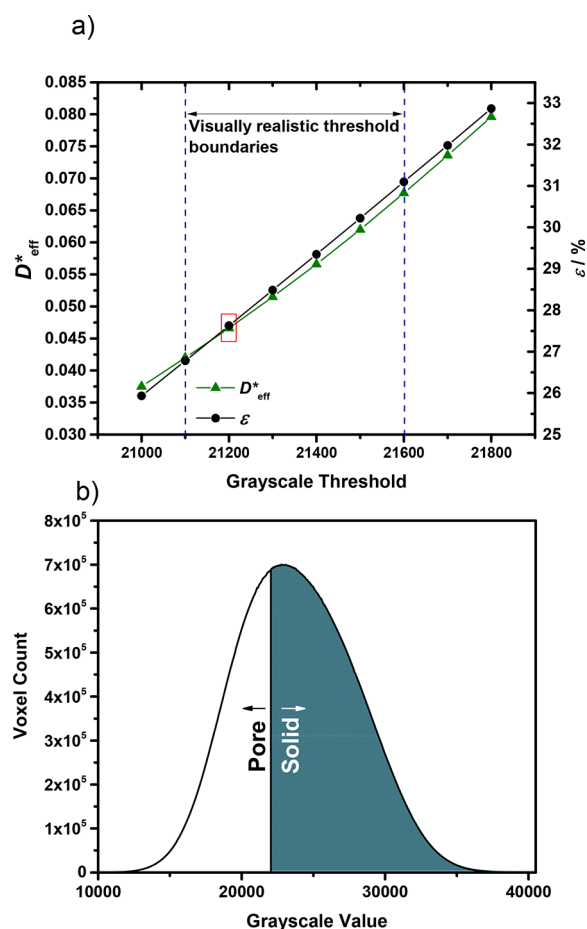


**Figure 3.** (a) Graph representing the variation in  $D^*_{\text{eff}}$  and porosity according to chosen grayscale value calculated with TauFactor. The red box indicates the threshold value chosen. (b) Overall histogram for the carbon and binder data set.

binder data set is presented in Figure 4 along with a 3D visualization of the segmented carbon and binder electrode. The value of  $D^*_{\text{eff}}$  was then calculated by running TauFactor on the segmented data set and found to be ca. 0.05.

It is worth noting that the morphology of the CBD porous network is highly dependent on the segmentation route chosen, and this in turn has a considerable effect on the diffusivity. This multi-instrument approach, combined with a sensitivity analysis, aims to address the uncertainties inherent in nano-CT when approaching its resolution limit.

The value for  $D^*_{\text{eff}}$  calculated previously for the stand-alone carbon and binder electrode was then used to determine the effective transport properties of the complete NMC electrode. The dimensions are  $190.2 \times 428.5 \times 34.9 \mu\text{m}^3$  (directions  $x$ ,  $y$ , and  $z$ , respectively) for the analyzed subvolume. The data set was segmented by thresholding the active NMC, carbon, and pore phases as shown in Figure 5. The calculated phase fractions for the three phases were 50, 36, and 14% for the NMC, CBD, and electrode macro-pores, respectively.

TauFactor was run in all three directions with two input data sets, namely, a two-phase and a three-phase segmentation. For the two-phase segmentation, the active material particles were segmented as shown in Figure 5 and the remaining pixels were assigned to a pore phase. The input parameters for the bulk diffusivities in TauFactor for this calculation were  $D^*_{\text{NMC}} = 0$  and  $D^*_{\text{pore}} = 1$ . For the three-phase segmentation shown in

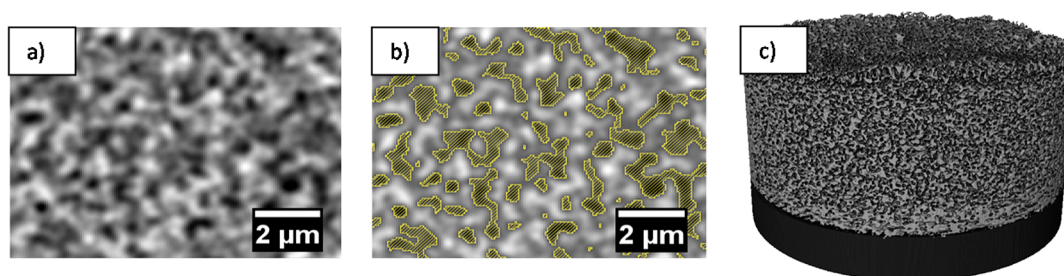


**Figure 4.** (a) Grayscale image extracted from the carbon and binder data set. (b) Segmented image extracted from the carbon and binder data set. (c) 3D representation of the complete carbon and binder data set.

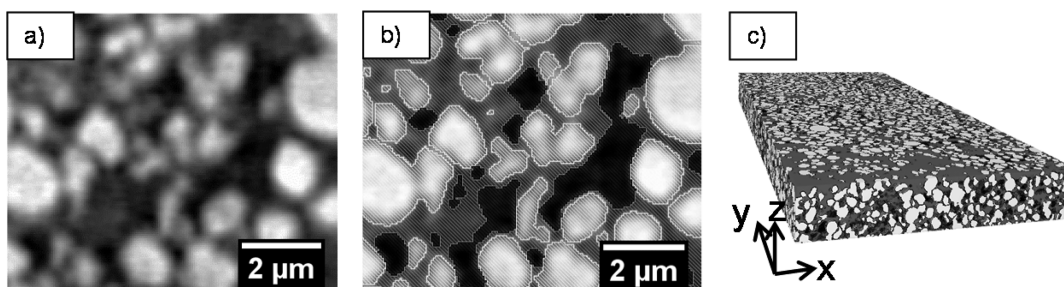


**Figure 5.** (a) Magnified grayscale image extracted from the NMC micro-CT data set. (b) Three-phase segmentation of the previous image. The white phase is the active material, the gray phase is the carbon and binder, and the black phase the macro-scale electrode pores. (c) 3D volume representing the subvolume used for transport simulations with the associated dimensions.

**Figure 5b**, two separate instances of TauFactor were run. In the first one, diffusion was only assumed to occur in the NMC macro-pores, with the input parameters  $D_{\text{NMC}}^* = 0$ ,  $D_{\text{CBD}}^* = 0$ , and  $D_{\text{pore}}^* = 1$ . In the second instance, the diffusivity calculated in the previous section is used as the input diffusivity for the CBD. The input parameters used are  $D_{\text{NMC}}^* = 0$ ,  $D_{\text{CBD}}^* = 0.05$ , and  $D_{\text{pore}}^* = 1$ .

The three-phase calculation outputs an effective diffusivity for the analyzed volume based on the overall flux through the control volume. However, this calculation omits information about the effective porosity of the CBD. An overall ensemble three-phase tortuosity factor for each direction can be calculated by a method presented by Cooper et al. by using eq 4:<sup>40</sup>

$$\tau = \frac{\epsilon_{\text{tot}}}{D^*} \quad (4)$$

where  $D_{\text{eff}}^*$  is the diffusivity obtained with the three-phase calculation from TauFactor for each direction and  $\epsilon_{\text{tot}}$  is given by the overall porosity of the electrode from the combination of the CBD porosity and the NMC electrode porosity by using eq 5:

$$\epsilon_{\text{tot}} = \epsilon_{\text{NMC}} + \phi_{\text{CBD}}\epsilon_{\text{CBD}} \quad (5)$$

where  $\epsilon_{\text{NMC}}$  is the NMC porosity,  $\phi_{\text{CBD}}$  is the CBD volume fraction, and  $\epsilon_{\text{CBD}}$  is the CBD porosity calculated in the previous section. All the resulting tortuosity factors are presented in **Figure 6**.

From the graph in **Figure 6**, a considerable increase in the tortuosity factor is observed when the CBD is considered and these values are consistent with previously observed values in the literature.<sup>31</sup> When a constricting CBD is introduced, the tortuosity increases considerably in all three directions and the values are less uniform. From **Figure 6**, it is possible to deduce that the extent to which  $\text{Li}^+$  ion diffusion is constricted depends on the diffusion path and how this is affected by the presence of a hindering phase such as the CBD: for example the effective tortuosity factor is highest for direction  $x$  with a value of 7.8

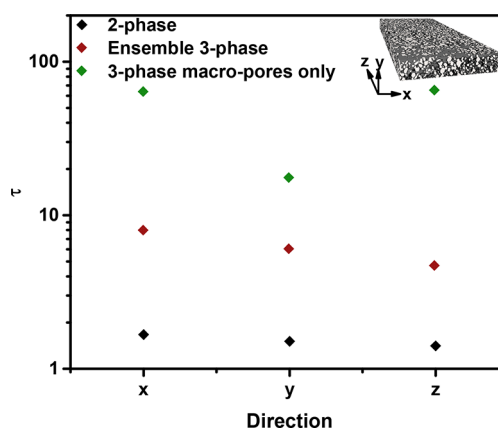


**Figure 6.** Graph representing the tortuosity factors calculated with TauFactor in three directions for the NMC micro-CT data set for the two-phase segmentation (black), ensemble three-phase scenario (red), and two-phase macro-pores (green).

where a combination of narrow diffusion pathways and obstructing phases (CBD and NMC) results in high tortuosity. The lowest value is of 4.6 in direction  $z$ , where the control volume edge length is also the shortest. These results could indicate that in the context of a thicker electrode, the spatial distribution of active and inactive phases needs to be tailored to obtain diffusion channels with a low tortuosity generated from a combination of larger and smaller pores for  $\text{Li}^+$  ions to travel throughout. When diffusion is considered solely in the NMC macro-pores, a considerable increase can be observed in all three directions, with values of 63.5, 17.4, and 64.9 in the  $x$ ,  $y$ , and  $z$  directions, respectively. This increase is due to the reduced percolation of the porous channels when the CBD is considered as a non-diffusive phase. These results indicate that a three-phase scenario yields results that are considerably different from simplified two-phase models and the influence of a diffusive

CBD must be taken into account. Further studies are required to quantify how the processing parameters such as slurry drying temperature can be related to the microstructural properties of the electrode and its intrinsic electrochemical performance.

Additional information regarding the porous network of the electrode was obtained by analyzing the results of the CPSD calculation to obtain an overall pore size distribution for both the CBD and the NMC pores.<sup>30,41</sup> This analysis is based on inscribing spheres of increasing diameter in the center of each pore. This is calculated by plotting a distance map from the pore walls; as the spheres grow, they fill a certain volume which is measured for each corresponding radius. This method allows analyzing continuous porous networks rather than using an equivalent spherical radius method that does not account for unusual and nonspherical pore shapes. Because this calculation outputs the pore volume, the CBD pore volume was inferior by several factors to the pore volume calculated for the NMC micro-CT data set due to the scale at which the data were collected and the overall sample size. The CBD volume contained in the NMC micro-CT data set was found to be ca. 36 times the volume of the analyzed nano-CT CBD subvolume. To have two comparable pore volume magnitudes, the carbon and binder nano-CT pore subvolume calculated via the CPSD approach was multiplied by a factor of 36. This was assumed valid based on the assumption that the nano-CT CBD data set was representative of the porous network as a whole; hence, the pore size distribution was assumed to be correct for the scaled data set. This procedure allows representing both the CBD and the NMC pore size distributions in a single graph as the percentage of the total pore volume of the electrode as presented in Figure 7.

From Figure 7, the average pore radii of ca. 180 nm and 1  $\mu\text{m}$  are observed for the nano- and micro-CT data sets, respectively.

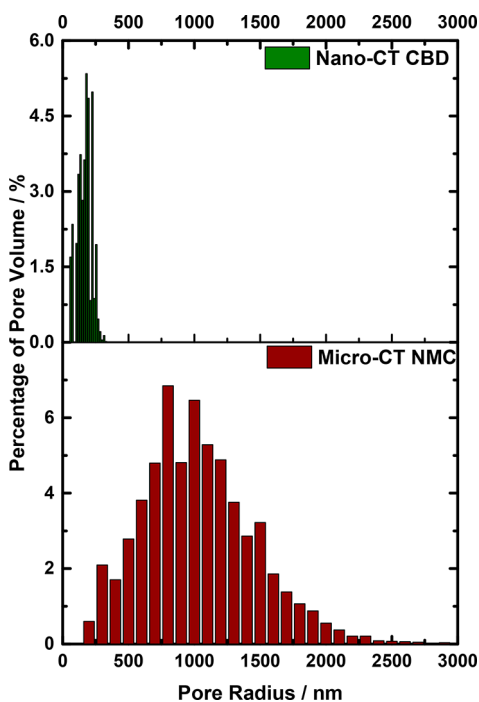


**Figure 7.** Continuous pore size distribution representing the pore radius versus the corresponding percentage of pore volume. Median pore radii of 180 nm and 1  $\mu\text{m}$  can be observed for the nano- and micro-CT, respectively.

The nano-CT porosity contributes to ca. 40% of the total pore volume whereas the remaining 60% of the pore volume is contributed to by pores within the spatial resolution of the micro-CT data. This indicates that both porosities are present in almost equal measure within the electrode and as such are thought to hold equal importance for the electrolyte interpenetration and diffusion purposes described previously.

Further quantification can be achieved by analyzing the pore throat equivalent radius distribution (Figure 8). Average

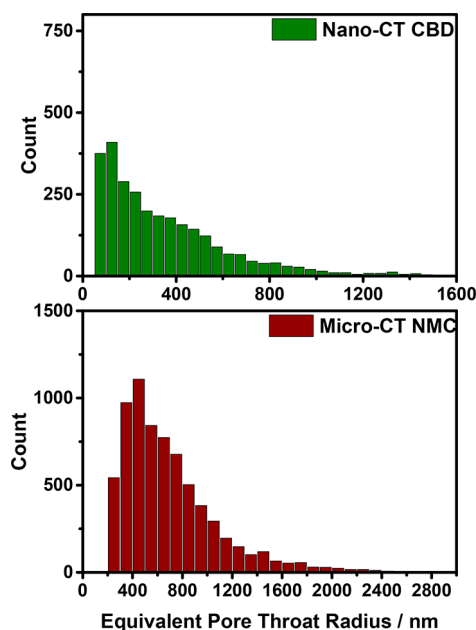


**Figure 8.** Pore throat equivalent radius distribution calculated for the nano-CT CBD and micro-CT NMC pores. Two distinct average pore throat sizes can be observed for the nano-CT and micro-CT data sets with values of ca. 350 and 700 nm, respectively.

equivalent radii of 350 and 700 nm can be observed for the nano-CT CBD and micro-CT NMC porous networks, respectively. The relevance of pore throats can be explained by examining their role in electrode wetting: electrolyte transport in porous network is both affected by the main pore cavities and the throats that connect these, and through this study, the size distributions across the two length scales can be observed.<sup>42</sup>

It is worth noting that the morphologies obtained in these electrodes and the results herein derived are specific to this electrode and are a direct consequence of the preparation techniques used, but the method described is widely applicable to a range of electrode chemistries and microstructures.

### 3. CONCLUSION

The correct characterization of the CBD is fundamental to fully understand transport phenomena within battery electrodes. To this end, we have devised a technique to directly image a carbon and binder layer with a combination of nano-CT and FIB-SEM. The nano-CT data set was used to provide a representative carbon and binder volume containing a characteristic porous network, whereas the FIB-SEM data were used to determine the porosity of the CBD and its morphology with regard to the overall electrode structure. This multimodal imaging approach, along with the expected porosity from mass calculations, was used to build a workflow which we believe enables a more

rational approach to threshold segmentation of three phase materials that are difficult to image. The effective diffusivity values calculated at the nano-scale were integrated into the larger NMC micro-CT data set which allowed the calculation of its multi-length scale ensemble tortuosity factor.

A comparison between the tortuosity factor calculated when considering or omitting the CBD in a 3D NMC electrode framework, pointed to a large increase in the tortuosity factor when the CBD is considered. A comparison was also drawn with a simplified two-phase scenario, where diffusion is only considered in the NMC macro-pores, yielding a considerably higher tortuosity factor. Furthermore, the results indicate that the arrangement of the connective porous network, made by the combination of larger macro-scale electrode pores and finer nano-scale CBD pores, is of utmost importance. These porous domains were also characterized via a CPSD approach that highlighted the pore sizes and how considerable amounts of the CBD and NMC pores are present in the electrode indicating that neither should be omitted. A size distribution for pore throats was also calculated, emphasizing the potential of this technique in analyzing microstructural properties of electrodes across different relevant length scales.

Improvements in this technique could be obtained with higher resolution lab-based nano-CT imaging, which has the potential to resolve smaller pores. However, in order to obtain a high-quality data set, it is necessary to tailor the sample to fit within the 16  $\mu\text{m}$  field-of-view. While the morphology of the CBD and electrode macro-pores may significantly change according to manufacturing technique, the approach presented in this work could be applied to a range of differently prepared materials.

## 4. METHODS

**Electrode and CBD Preparation.** In order to effectively characterize the influence of the CBD layer, two samples have been prepared: a functioning NMC electrode and a stand-alone CBD layer. The CBD layer was prepared by homogenizing conductive carbon black (Timcal Super C65, Imerys, Switzerland) and poly(vinylidene fluoride) binder (PVDF) (Arkema, France) in a 50:50 weight ratio. *N*-Methyl-2-pyrrolidinone (NMP; anhydrous, Sigma-Aldrich) was used as a solvent, and the slurry was then spread onto aluminum foil with a doctor blade with a 250  $\mu\text{m}$  blade gap and dried in a vacuum oven overnight at 80  $^{\circ}\text{C}$ .

The NMC electrode utilized was prepared as described in a previous publication.<sup>43</sup> The mass ratios utilized for this electrode were 90:5:5 for NMC111 (Targray, Canada), conductive carbon black (TimcalSuper C65), and PVDF. These were homogenized using a dual asymmetric centrifuge system (SpeedMixer DAC 150.1 FVZ-K, Hauschild, Germany) and NMP as a solvent. The slurry was cast onto an aluminum foil and dried overnight at 80  $^{\circ}\text{C}$ .

**X-ray nano-CT.** The stand-alone CBD layer was micromachined into a micro-scale pillar: a 1 mm electrode disk was cut out with the aid of a biopsy punch, which was then glued onto a 1 mm pin using a two-part epoxy. This was then successively milled down with a laser micromachining instrument (A Series/Compact Laser Micromachining System, Oxford Lasers) to a ca. 100  $\mu\text{m}$  diameter pillar. Further details about sample preparation can be found elsewhere.<sup>44</sup>

The samples were scanned using a lab nano-CT instrument (Xradia Ultra 810, Carl Zeiss Inc.) utilizing a microfocus rotating anode X-ray source (MicroMax-007HF, Rigaku) with the tube voltage set at 35 kV and current at 25 mA, in X-ray Zernike phase contrast mode.<sup>45</sup> In large field-of-view mode with no pixel binning the resultant effective pixel size of ca. 63 nm was achieved across a field-of-view of 65  $\mu\text{m}$ . The exposure time was set to 45 s, and 1601 projections were taken. The radiographs were reconstructed in a 3D volume using a filtered back-projection algorithm implemented in the commercially available Zeiss XMReconstructor (Carl Zeiss Inc.).

**X-ray micro-CT.** A small triangle was cut from the full NMC electrode and characterized with a lab-based micro-CT instrument (Xradia Versa 520, Carl Zeiss Inc.), with an 80 kV tube voltage and 40 $\times$  optical magnification. Using no pixel binning, the resultant effective pixel size of 237 nm was achieved across a field-of-view of ca. 400  $\mu\text{m}$ . 3201 projections were captured with 60 s exposure time per projection. The radiographs were reconstructed in a 3D volume using a filtered back-projection algorithm (FDK<sup>46</sup>) implemented in the commercially available Zeiss XMReconstructor (Carl Zeiss Inc.).

**FIB-SEM Imaging.** FIB-SEM analysis was carried out on a ZEISS Crossbeam 340. A focused Ga<sup>+</sup> ion beam was used to mill trenches into the electrode surface: a Pt protective layer was deposited locally using the single needle gas injection system (GIS); subsequently a series of three milling steps using FIB currents of 30, 7, and 3 nA were carried out to provide a polished cross-section for SEM imaging. SEM images were recorded with 3072  $\times$  2304 pixels at 1 keV electron beam energy using the secondary electron (SE) detector as well as the in-lens backscatter electron (BSE) detector.

**Image Visualization, Segmentation, and Analysis.** Image visualization and segmentation were performed on the reconstructed data sets with Avizo (Visualization Sciences Group, FEI Co.) and MATLAB. For the nano-CT CBD data, a subsection completely internal to the CBD electrode of 265  $\times$  645  $\times$  618 voxels was selected, corresponding to a volume of ca. 16.7  $\times$  40.6  $\times$  38.9  $\mu\text{m}^3$  (ca. 3  $\times$  10<sup>-5</sup> mm<sup>3</sup>). A range of threshold values were then used for segmentation by using a custom MATLAB script. TauFactor<sup>35</sup> was then used to determine the tortuosity factor and the effective diffusivity of the porous network within the CBD, and the CPSD was calculated using the Beat plugin in ImageJ.<sup>41</sup> The FIB-SEM images of the full NMC electrode were extracted with ImageJ and thresholded in Avizo, where the porosity was also calculated.

From the micro-CT NMC data set, a subvolume of 801  $\times$  147  $\times$  1804 voxels corresponding to a volume of ca. 190.2  $\times$  34.9  $\times$  428.5  $\mu\text{m}^3$  (ca. 3  $\times$  10<sup>-3</sup> mm<sup>3</sup>) was extracted. The segmentation was carried out in Avizo using thresholding. A series of erosion and dilation operations were sequentially used to eliminate any interfacial artifacts between the particle and pore phases caused by the partial volume effect. The tortuosity factor was again calculated with TauFactor, and the CPSD was calculated in ImageJ.<sup>35,41</sup> A representative volume element analysis was carried out in TauFactor for both nano- and micro-CT data sets for the porosity and tortuosity factors to ensure that the volumes are representative. The pore throat distribution was obtained by running the XPoreNetworkModeling extension in Avizo on both the nano- and micro-CT data sets. The resulting radii below the pixel resolution for each data set were regarded as artifacts and discarded.

## AUTHOR INFORMATION

### Corresponding Author

\*E-mail: p.shearing@ucl.ac.uk.

### ORCID

Paul R. Shearing: 0000-0002-1387-9531

### Notes

The authors declare no competing financial interest.

## ACKNOWLEDGMENTS

We acknowledge funding from the Engineering and Physical Sciences Research Council (EPSRC; Grants EP/N032888/1, EP/K005030/1, and EP/M009394/1), the Royal Academy of Engineering. S.R.D. acknowledges EPSRC and Johnson Matthey for funding via the CASE studentship scheme.

## REFERENCES

- (1) Nitta, N.; Wu, F.; Lee, J. T.; Yushin, G. Li-Ion Battery Materials: Present and Future. *Mater. Today* **2015**, *18* (5), 252–264.
- (2) Marks, T.; Trussler, S.; Smith, A. J.; Xiong, D.; Dahn, J. R. A Guide to Li-Ion Coin-Cell Electrode Making for Academic Researchers. *J. Electrochem. Soc.* **2011**, *158* (1), A51–A57.

- (3) Thorat, I. V.; Stephenson, D. E.; Zacharias, N. A.; Zaghbi, K.; Harb, J. N.; Wheeler, D. R. Quantifying Tortuosity in Porous Li-Ion Battery Materials. *J. Power Sources* **2009**, *188* (2), 592–600.
- (4) Chen, Y.-H.; Wang, C.-W.; Liu, G.; Song, X.-Y.; Battaglia, V. S.; Sastry, a. M. Selection of Conductive Additives in Li-Ion Battery Cathodes. *J. Electrochem. Soc.* **2007**, *154* (10), A978.
- (5) Doyle, M.; Fuller, T. F.; Newman, J. S. Modeling of Galvanostatic Charge and Discharge of the Lithium/Polymer/Insertion Cell. *J. Electrochem. Soc.* **1993**, *140* (6), 1526.
- (6) Kehrwald, D.; Shearing, P. R.; Brandon, N. P.; Sinha, P. K.; Harris, S. J. Local Tortuosity Inhomogeneities in a Lithium Battery Composite Electrode. *J. Electrochem. Soc.* **2011**, *158* (12), A1393.
- (7) Arakawa, M.; Tobishima, S.; Nemoto, Y.; Ichimura, M.; Yamaki, J. Lithium Electrode Cycleability and Morphology Dependence on Current Density. *J. Power Sources* **1993**, *43* (1–3), 27–35.
- (8) Chen, D.; Indris, S.; Schulz, M.; Gamer, B.; Mönig, R. In Situ Scanning Electron Microscopy on Lithium-Ion Battery Electrodes Using an Ionic Liquid. *J. Power Sources* **2011**, *196* (15), 6382–6387.
- (9) Osaka, T.; Homma, T.; Momma, T.; Yarimizu, H. In Situ Observation of Lithium Deposition–Recesses in Solid Polymer and Gel Electrolytes. *J. Electroanal. Chem.* **1997**, *421*, 153–156.
- (10) Song, B.; Sui, T.; Ying, S.; Li, L.; Lu, L.; Korsunsky, A. Nano-Structural Changes in Li-Ion Battery Cathode during Cycling Revealed by FIB-SEM Serial Sectioning Tomography. *J. Mater. Chem. A* **2015**, *3*, 18171–18179.
- (11) Vierrath, S.; Zielke, L.; Moroni, R.; Mondon, A.; Wheeler, D. R.; Zengerle, R.; Thiele, S. Morphology of Nanoporous Carbon-Binder Domains in Li-Ion Batteries - A FIB-SEM Study. *Electrochem. Commun.* **2015**, *60*, 176–179.
- (12) Ender, M.; Joos, J.; Carraro, T.; Ivers-Tiffée, E. Quantitative Characterization of LiFePO<sub>4</sub> Cathodes Reconstructed by FIB/SEM Tomography. *J. Electrochem. Soc.* **2012**, *159* (7), A972–A980.
- (13) Hutzenlaub, T.; Asthana, a.; Becker, J.; Wheeler, D. R.; Zengerle, R.; Thiele, S. FIB/SEM-Based Calculation of Tortuosity in a Porous LiCoO<sub>2</sub> Cathode for a Li-Ion Battery. *Electrochem. Commun.* **2013**, *27*, 77–80.
- (14) Balke, N.; Jesse, S.; Morozovska, a. N.; Eliseev, E.; Chung, D. W.; Kim, Y.; Adamczyk, L.; García, R. E.; Dudney, N.; Kalinin, S. V. Nanoscale Mapping of Ion Diffusion in a Lithium-Ion Battery Cathode. *Nat. Nanotechnol.* **2010**, *5* (10), 749–754.
- (15) Chung, D.-W.; Balke, N.; Kalinin, S. V.; Edwin García, R. Virtual Electrochemical Strain Microscopy of Polycrystalline LiCoO<sub>2</sub> Films. *J. Electrochem. Soc.* **2011**, *158* (10), A1083.
- (16) Balke, N.; Jesse, S.; Kim, Y.; Adamczyk, L.; Ivanov, I. N.; Dudney, N. J.; Kalinin, S. V. Decoupling Electrochemical Reaction and Diffusion Processes in Ionically-Conductive Solids on the Nanometer Scale. *ACS Nano* **2010**, *4* (12), 7349–7357.
- (17) Shanti, N. O.; Chan, V. W. L.; Stock, S. R.; De Carlo, F.; Thornton, K.; Faber, K. T. X-Ray Micro-Computed Tomography and Tortuosity Calculations of Percolating Pore Networks. *Acta Mater.* **2014**, *71*, 126–135.
- (18) Yermukhambetova, A.; Tan, C.; Daemi, S. R.; Bakenov, Z.; Darr, J. A.; Brett, D. J. L.; Shearing, P. R. Shearing, Exploring 3D Microstructural Evolution in Li-Sulfur Battery Electrodes Using in-Situ X-Ray Tomography. *Sci. Rep.* **2016**, *6* (1), 35291.
- (19) Ebner, M.; Geldmacher, F.; Marone, F.; Stamparoni, M.; Wood, V. X-Ray Tomography of Porous, Transition Metal Oxide Based Lithium Ion Battery Electrodes. *Adv. Energy Mater.* **2013**, *3* (7), 845–850.
- (20) Chen-Wiegart, Y. K.; Liu, Z.; Faber, K. T.; Barnett, S. a.; Wang, J. 3D Analysis of a LiCoO<sub>2</sub>–Li(Ni<sub>1/3</sub>Mn<sub>1/3</sub>Co<sub>1/3</sub>)O<sub>2</sub> Li-Ion Battery Positive Electrode Using X-Ray Nano-Tomography. *Electrochem. Commun.* **2013**, *28*, 127–130.
- (21) Yan, B.; Lim, C.; Yin, L.; Zhu, L. Three Dimensional Simulation of Galvanostatic Discharge of LiCoO<sub>2</sub> Cathode Based on X-Ray Nano-CT Images. *J. Electrochem. Soc.* **2012**, *159* (10), A1604–A1614.
- (22) Finegan, D. P.; Scheel, M.; Robinson, J. B.; Tjaden, B.; Hunt, I.; Mason, T. J.; Millichamp, J.; Di Michiel, M.; Offer, G. J.; Hinds, G.; Brett, D. J. L.; Shearing, P. R. In-Operando High-Speed Tomography of Lithium-Ion Batteries during Thermal Runaway. *Nat. Commun.* **2015**, *6*, 6924.
- (23) Zielke, L.; Barchasz, C.; Waluś, S.; Alloin, F.; Leprêtre, J.-C.; Spetl, A.; Schmidt, V.; Hilger, A.; Manke, I.; Banhart, J.; Zengerle, R.; Thiele, S. Degradation of Li/S Battery Electrodes On 3D Current Collectors Studied Using X-Ray Phase Contrast Tomography. *Sci. Rep.* **2015**, *5* (April), 10921.
- (24) Shearing, P. R.; Howard, L. E.; Jørgensen, P. S.; Brandon, N. P.; Harris, S. J. Characterization of the 3-Dimensional Microstructure of a Graphite Negative Electrode from a Li-Ion Battery. *Electrochem. Commun.* **2010**, *12* (3), 374–377.
- (25) Shearing, P. R.; Brandon, N. P.; Gelb, J.; Bradley, R.; Withers, P. J.; Marquis, a. J.; Cooper, S.; Harris, S. J. Multi Length Scale Microstructural Investigations of a Commercially Available Li-Ion Battery Electrode. *J. Electrochem. Soc.* **2012**, *159* (7), A1023–A1027.
- (26) Withers, P. J. X-Ray Nanotomography. *Mater. Today* **2007**, *10* (12), 26–34.
- (27) Landis, E. N.; Keane, D. T. X-Ray Microtomography. *Mater. Charact.* **2010**, *61* (12), 1305–1316.
- (28) Cooper, S. J.; Eastwood, D. S.; Gelb, J.; Damblanc, G.; Brett, D. J. L.; Bradley, R. S.; Withers, P. J.; Lee, P. D.; Marquis, a. J.; Brandon, N. P.; Shearing, P. R. Image Based Modelling of Microstructural Heterogeneity in LiFePO<sub>4</sub> Electrodes for Li-Ion Batteries. *J. Power Sources* **2014**, *247*, 1033–1039.
- (29) Chung, D.-W.; Ebner, M.; Ely, D. R.; Wood, V.; Edwin García, R. Validity of the Bruggeman Relation for Porous Electrodes. *Modell. Simul. Mater. Sci. Eng.* **2013**, *21* (7), 074009.
- (30) Taiwo, O. O.; Finegan, D. P.; Eastwood, D. S.; Fife, J. L.; Brown, L. D.; Darr, J. A.; Lee, P. D.; Brett, D. J. L.; Shearing, P. R. Comparison of Three-Dimensional Analysis and Stereological Techniques for Quantifying Lithium-Ion Battery Electrode Microstructures. *J. Microsc.* **2016**, *263* (3), 280–292.
- (31) Hutzenlaub, T.; Asthana, A.; Becker, J.; Wheeler, D. R.; Zengerle, R.; Thiele, S. FIB/SEM-Based Calculation of Tortuosity in a Porous LiCoO<sub>2</sub> Cathode for a Li-Ion Battery. *Electrochem. Commun.* **2013**, *27*, 77–80.
- (32) Hutzenlaub, T.; Thiele, S.; Paust, N.; Spotnitz, R.; Zengerle, R.; Walchshofer, C. Three-Dimensional Electrochemical Li-Ion Battery Modelling Featuring a Focused Ion-Beam/scanning Electron Microscopy Based Three-Phase Reconstruction of a LiCoO<sub>2</sub> Cathode. *Electrochim. Acta* **2014**, *115*, 131–139.
- (33) Zielke, L.; Hutzenlaub, T.; Wheeler, D. R.; Manke, I.; Arlt, T.; Paust, N.; Zengerle, R.; Thiele, S. A Combination of X-Ray Tomography and Carbon Binder Modeling: Reconstructing the Three Phases of LiCoO<sub>2</sub> Li-Ion Battery Cathodes. *Adv. Energy Mater.* **2014**, *4* (8), 1301617.
- (34) Zielke, L.; Hutzenlaub, T.; Wheeler, D. R.; Chao, C.-W.; Manke, I.; Hilger, A.; Paust, N.; Zengerle, R.; Thiele, S. Three-Phase Multiscale Modeling of a LiCoO<sub>2</sub> Cathode: Combining the Advantages of FIB-SEM Imaging and X-Ray Tomography. *Adv. Energy Mater.* **2015**, *5* (5), 1401612.
- (35) Cooper, S. J.; Bertei, A.; Shearing, P. R.; Kilner, J. A.; Brandon, N. P. TauFactor: An Open-Source Application for Calculating Tortuosity Factors from Tomographic Data. *SoftwareX* **2016**, *5*, 203–210.
- (36) Moroni, R.; Börner, M.; Zielke, L.; Schroeder, M.; Nowak, S.; Winter, M.; Manke, I.; Zengerle, R.; Thiele, S. Multi-Scale Correlative Tomography of a Li-Ion Battery Composite Cathode. *Sci. Rep.* **2016**, *6*, 30109.
- (37) Vu, A.; Qian, Y.; Stein, A. Porous Electrode Materials for Lithium-Ion Batteries-How to Prepare Them and What Makes Them Special. *Adv. Energy Mater.* **2012**, *2* (9), 1056–1085.
- (38) MTI TIMICAL Super C65 Specification; MTI, <http://www.mtixl.com/TimicalSUPER65forLithium-IonBatteries80g/bag-EQ-Lib-SuperC65.aspx> (accessed Jan. 2, 2018).
- (39) Hess, W.; Herd, C. Microstructure, Morphology and General Physical Properties. In *Carbon Black: Science and Technology*, 2nd ed.; Donnet, J.-B., Ed.; CRC Press, 1993; p 121.
- (40) Cooper, S. J.; Li, T.; Bradley, R. S.; Li, K.; Brandon, N. P.; Kilner, J. A. Multi Length-Scale Quantification of Hierarchical Microstructure

in Designed Microtubular SOFC Electrodes. *ECS Trans.* **2015**, *68* (1), 1857–1864.

(41) Münch, B.; Holzer, L. Contradicting Geometrical Concepts in Pore Size Analysis Attained with Electron Microscopy and Mercury Intrusion. *J. Am. Ceram. Soc.* **2008**, *91* (12), 4059–4067.

(42) Sheng, Y.; Fell, C. R.; Son, Y. K.; Metz, B. M.; Jiang, J.; Church, B. C. Effect of Calendering on Electrode Wettability in Lithium-Ion Batteries. *Front. Energy Res.* **2014**, *2*, 00056.

(43) Randjbar Daemi, S.; Brett, D. J. L.; Shearing, P. R. A Lab-Based Multi-Length Scale Approach to Characterize Lithium-Ion Cathode Materials. *ECS Trans.* **2017**, *77* (11), 1119–1124.

(44) Bailey, J. J.; Heenan, T. M. M.; Finegan, D. P.; Lu, X.; Daemi, S. R.; Iacoviello, F.; Backeberg, N. R.; TAIWO, O. O.; BRETT, D. J. L.; ATKINSON, A.; SHEARING, P. R. Laser-Preparation of Geometrically Optimised Samples for X-Ray Nano-CT. *J. Microsc.* **2017**, *267* (3), 384–396.

(45) Eastwood, D. S.; Bradley, R. S.; Tariq, F.; Cooper, S. J.; Taiwo, O. O.; Gelb, J.; Merkle, a.; Brett, D. J. L.; Brandon, N. P.; Withers, P. J.; Lee, P. D.; Shearing, P. R. The Application of Phase Contrast X-Ray Techniques for Imaging Li-Ion Battery Electrodes. *Nucl. Instrum. Methods Phys. Res., Sect. B* **2014**, *324*, 118–123.

(46) Feldkamp, L. A.; Davis, L. C.; Kress, J. W. Practical Cone-Beam Algorithm. *J. Opt. Soc. Am. A* **1984**, *1* (6), 612–619.